Supporting Information

Tailoring MXene-based Film as a Moisture-Responsive Actuator for Continuous Energy Conversion

Luyu Yang, Lei Zhang*, Jian Cui, and Dongping Sun*

Institute of Chemicobiology and Functional Materials, School of Chemistry and Chemical Engineering, Nanjing University of Science and Technology, 200 Xiao Ling Wei, Nanjing 210094, China.

*Corresponding author, E-mail:
sundpe301@163.com (Dongping Sun);
leizhang@njust.edu.cn (Lei Zhang).

Experimental Section

Materials

Ti_3AlC_2 MAX powder (400 mesh) was purchased from Jilin 11 technology Co., Ltd. (China). The large-sized graphene oxide (1 μm < lateral dimensions < 50 μm, 99.9%) was purchased from Xianfeng Nano Co., Ltd. (China). The piezoelectric poly(vinylidene fluoride) (PVDF, d_{33}=35 pC/N) film was purchased from KUREHA (Japan). Lithium fluoride (LiF, 99.9%), hydrochloric acid (HCl, 37 wt %), L-ascorbic acid (L-AA, 99 wt %), and dopamine hydrochloride (DA, 98%) were purchased from Sinopharm Chemical Reagent Co., Ltd. (China). All chemicals or materials were directly used without further treatment.

Preparation of $Ti_3C_2T_X$ MXene dispersion:

The monolayer $Ti_3C_2T_x$ MXene was obtained by selectively etching Ti_3AlC_2 MAX with HCl/LiF as previously described.[1] Typically, 2 g of Ti_3AlC_2 powder was added to 35 mL of HCl solution (12 M), to which 2 g of LiF has been dissolved ahead. The mixture was stirred at 35 °C for 30 h. After complete reaction, the product was centrifuged (7500 rpm, 10 min) and washed repeatedly with deionized water till the pH of the supernatant was larger than 6.0. Subsequently, the precipitate was redispersed in deionized water and sonicated in ice water bath for 1 hour under N_2 atmosphere, followed by centrifugation (3500 rpm, 5 minutes) to obtaine exfoliated $Ti_3C_2T_x$ MXene supernatant with a dark-green color and a concentration of 2−5 mg mL^{-1}.

Preparation of rGO dispersion

The rGO was prepared by using the green reducing reagent L-AA.[2] In detail, L-AA was added into GO nanosheet suspension (0.2 mg/mL) and sonicated at low temperature for 10 minutes (the mass ratio of GO/L-AA is 1:5). Then the mixture was transferred to a water bath at 65°C for 1, 2, 3, 4, and 5 h without stirring. The prepared rGO was washed/centrifuged to remove residual ions, and then redispersed by ultrasound sonication to obtain rGO dispersion with a concentration of about 0.5 mg mL^{-1}. The resulting product was named rGO_x, where x was 1, 2, 3, 4, or 5, respectively.

Preparation of PD-rGOMX film

The PD-rGOMX film was obtained by vacuum-assisted filtration of the PDA-treated rGO/MXene dispersion. In a typical procedure, dopamine solution was added to the prepared mixed dispersion of rGO and MXene. Afterward, the solution was stirred for 4 h at room temperature until the reaction was completed. The PD-rGOMX films were obtained by vacuum-assisted filtration of the mixture, fixed within two cellulose filter papers, and dried naturally in the air at room temperature to prevent curling during the drying process. By changing the mass ratio of rGO/MXene to DA, we obtained PD-rGOMX films with different amounts of PDA. The preparation of GO film, rGO film, MXene film, and rGO/MXene film followed the same procedures. GO/MXene film was also prepared by vacuum-assisted filtration of mixed solution of GO and MXene (60 wt%).

Preparation of Moisture-driven generator

First, the 24 μm thick PVDF films were cleaned with ethanol and immediately coupled with the PD-rGOMX film, by applying a small amount of conductive silver paint to a random spot on the edge of the film to combine the PVDF and PD-rGOMX film. As shown in Fig. S20, a metal electrode was deposited on one side of the PVDF film. Finally, two copper wires were glued separately to the surfaces of PD-rGOMX film electrode and the metal electrode by the conductive silver paint.

Characterizations and Measurement

Scanning electron microscope (SEM, JSM-IT500HR), atomic force microscopy (AFM, Bruker Veeco Multimode 8), and high-resolution transmission electron microscope (HRTEM, FEI Tecnai F20) were used to study the morphology and microstructure of the as-pr Conductivities epared samples. The chemical structures of the as-prepared samples were obtained by Raman spectrometer (Aramis, Horiba Jobin Yvon), X-ray photoelectron spectroscopy (XPS, PHI Quantera II), and UV-vis absorption spectrometer (Evolution 220). The contact angles of the as-prepared samples were measured using a video optical contact angle meter (Dataphysics OCA25L, Germany). X-ray diffraction (XRD) spectra were collected by the D8 Advance X-diffractometer (Bruker AXS) with Cu Kα radiation ($\lambda = 1.5418$ Å) in the range $5° < 2\theta < 80°$ and a scan rate of 5°/min. The conductivity (σ) of the prepared samples was measured by the standard four-probe method. The electrochemical workstation (CS235OH, CORRTEST instruments) records all voltage and current signals. Mechanical properties of the as-prepared samples were measured by an electronic universal testing machine (TY8000-A, 1 mm min^{-1}). The thickness of the film is calculated with a micrometer. All videos and optical photos were recorded with an iphone 12 (Apple).

The volunteers who participated in Fig.s 4-6 are also co-authors of this manuscript. Informed consent was obtained from all volunteers and ethical approval was not required.

Water Absorption and Dehydration Experiment of the PD-rGOMX film

Placing the PD-rGOMX film in a confined space containing 35°C water and 100% RH, we measured the thickness and quality of the film at regular intervals. Specifically, use a helical micrometer and an analytical balance to measure regularly and quickly.

Moisture Response Experiment of the PD-rGOMX film

We artificially created an environment with steady humidity gradient on top of the nylon mesh by controlling the water temperature underneath (water temperature 35°C, ΔRH about 45%). The movement of the PD-rGOMX film on the top surface of the nylon mesh was recorded by an iPhone 12 recording. Here, we define the bending angle as the angle between the line connecting the two endpoints of the free moving film and the horizontal line. The response time is defined as the time required for the film to complete the maximum bending from the unbent state under the humidity gradient, and the recovery time as the time required for the film to reach the unbent state from the maximum bending angle during natural dehydration.

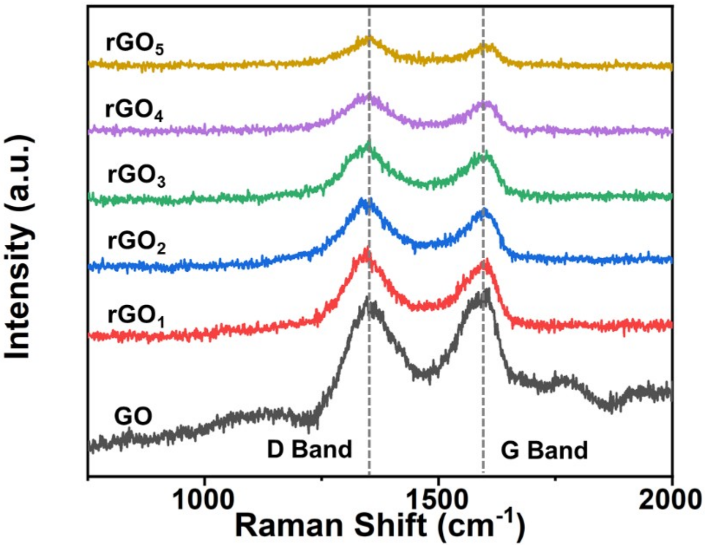

Fig. S1 Raman spectra of GO and rGO$_1$−rGO$_5$. With the extension of the reduction time, the ratio of the intensities of I_D/I_G (1329 and 1589 cm^{-1}) gradually increases (Table S1), revealing an increase in the level of defects and the formation of new sp^2 domains. [3, 4]

Table S1. I_D/I_G ratios of GO and rGO with different reduction time.

Materials	GO	rGO$_1$	rGO$_2$	rGO$_3$	rGO$_4$	rGO$_5$
I_D/I_G	0.97	1.08	1.13	1.17	1.2	1.22

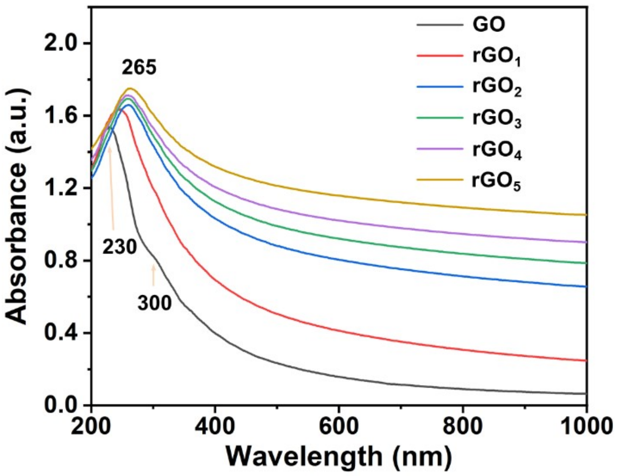

Fig. S2 UV-vis spectra of GO and rGO$_1$−rGO$_5$. UV-Vis spectra (Fig. 2e) show that all rGO samples have been observed with significant peak shifts compared to GO. The absorption peak of GO is centered at 230 nm, which is attributed to the π-π* transition of the aromatic C=C bond, and 300 nm is the n-π* transition of the C=O bond.[5] For the rGO samples, the peaks are concentrated near 265 nm, indicating successful reduction of the samples. In addition, the absorption intensity above 300 nm increases significantly with the extension of reduction time, indicating reduced GO with recovered aromatic structures.[6]

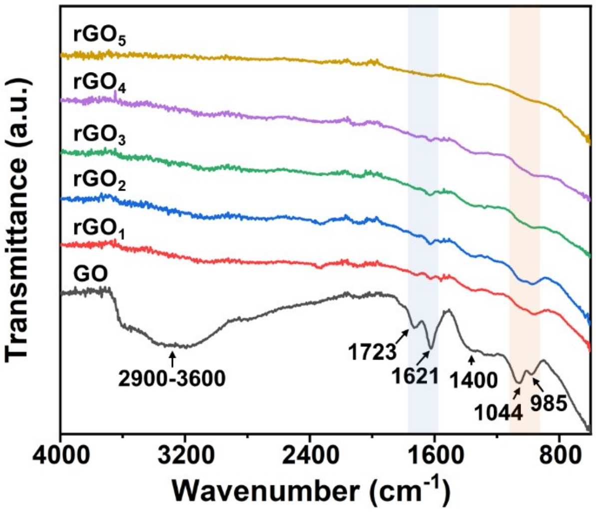

Fig. S3 FTIR spectra of GO and rGO$_1$-rGO$_5$. A broad, intense band at 2900-3600 cm^{-1} (O-H stretching vibrations) and narrower bands at about 1720 cm^{-1} (C=O stretching vibrations from carbonyl and carboxyl groups), 1620 cm^{-1} (C=C stretching, skeletal vibrations from unoxidized graphitic domains), 1400 cm^{-1} (O-H bending vibrations from hydroxyl groups), 1044 cm^{-1} (breathing vibrations from epoxy groups), and 980 cm^{-1} (attributed to vibrations from epoxy, ether or peroxide groups).[7-9] For all the reduced materials (rGO$_1$-rGO$_5$), the intensities of the bands associated to oxygen functional groups strongly decrease in relation to those of unreduced graphene oxide.[10] However, the elimination of these bands is not complete, as becomes evident when comparing the spectra of samples rGO$_1$-rGO$_3$ with that of pristine graphite. In particular, the persistence of the band at about 980-1044 cm^{-1} would seem to imply that a certain fraction of oxygen functional groups remained even in the most reduced dispersions.

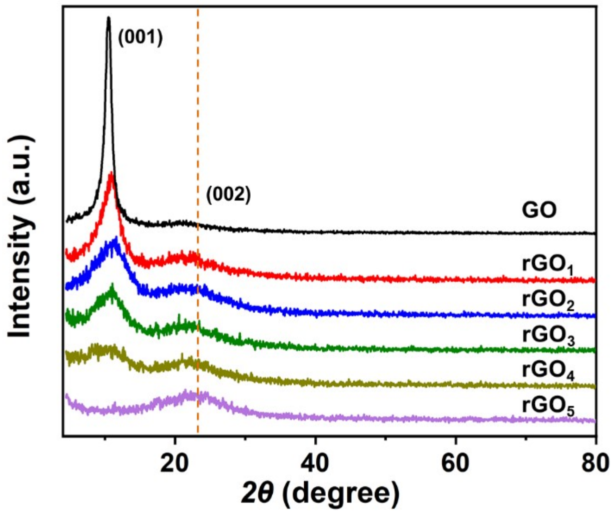

Fig. S4 XRD patterns of GO and rGO_1-rGO_5. The peak at $2\theta = 10.06°$ corresponds to the (100) plane of GO and the interplanar spacing is calculated to be 0.86 nm according to the Bragg equation. For rGO_1-rGO_5, the diffraction peak around 10.06° gradually weakened and finally disappeared with the prolongation of reduction time, and a relatively broad diffraction peak appears near 24.2°, and its interplanar spacing was about 0.33 nm. The results show that after reduction, the functional groups of GO, especially the functional groups between layers gradually disappear, resulting in the interlayer spacing of rGO being smaller than that of GO, confirms that the reduction of GO can be well-controlled by adjusting the reduction time.

Table S2. C/O ratios (XPS) of GO and rGO with different reduction time.

Materials	GO	rGO$_1$	rGO$_2$	rGO$_3$	rGO$_4$	rGO$_5$
C/O ratio	2.07	2.26	2.59	3.16	3.72	4.05

The increased C/O ratio from 2.07 to 4.05 derived from X-ray photoelectron spectroscopy (XPS) indicates the loss of oxygen-containing functional groups, *i.e.*, the reduction of GO.

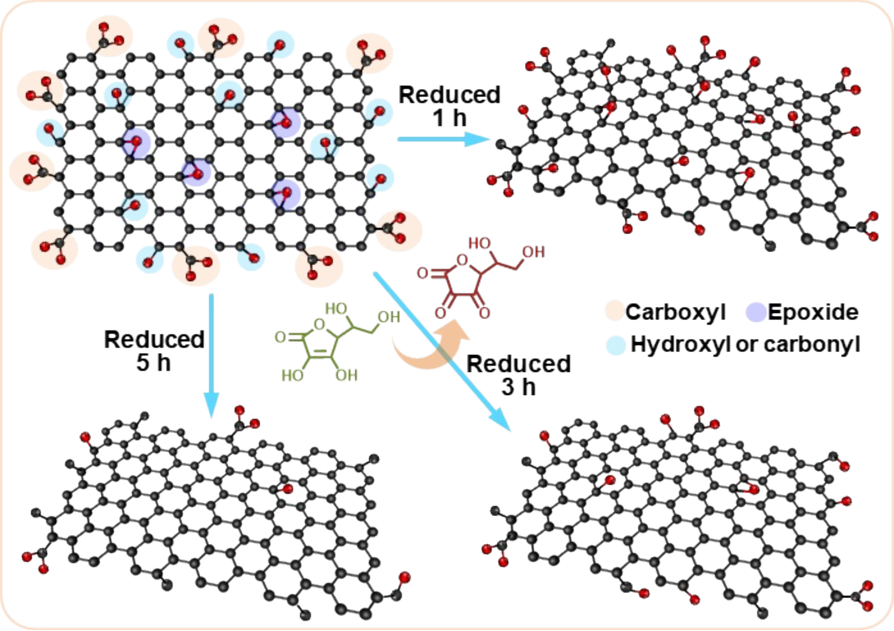

Fig. S5 Schemes showing the oxygen functional groups after reduction of GO by ascorbic acid for 1 h, 3 h, and 5 h. Oxygen-containing functional groups are attached to both the edges and the surface of GO. When GO is reduced by L-ascorbic acid, oxygen-containing functional groups such as hydroxyl and epoxide gradually disappear as the reduction time increases. Hydroxyl and epoxy compounds mainly fixed on the base surface are first reduced, while the carboxyl and carbonyl groups mainly located at the edges are more difficult to be reduced.

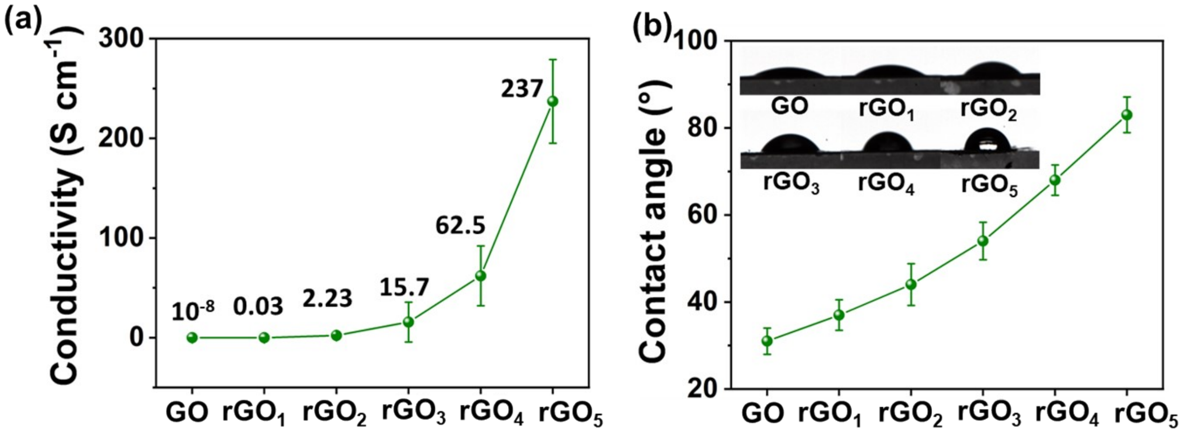

Fig. S6 a) Conductivities and b) contact angles of GO and rGO1−rGO5 films. Both the conductivity and water contact angle of rGO increase with the extension of the reduction time.

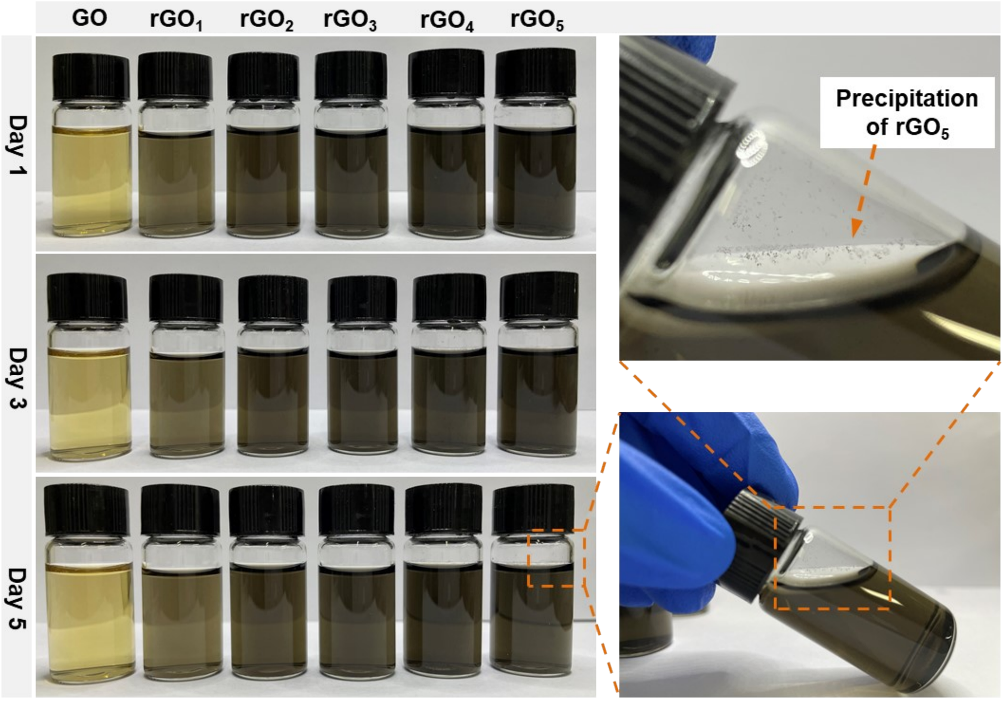

Fig. S7 Optical images of GO and rGO dispersions with different degrees of reduction kept at room temperature for 1, 3 and 5 days. We re-dispersed the rGO_1−rGO_5 samples in water after the ultrasound sonication, and found that rGO_1−rGO_3 were more stable in water, while rGO_5

had poorer stability, suggesting the hydrophilic functional groups were largely retained in rGO_1–rGO_3.

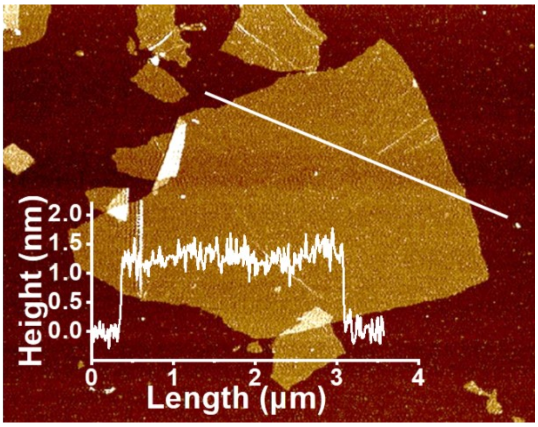

Fig. S8 AFM image of GO nanoflakes shows an ultrathin structure with a thickness of about 1.2 nm.

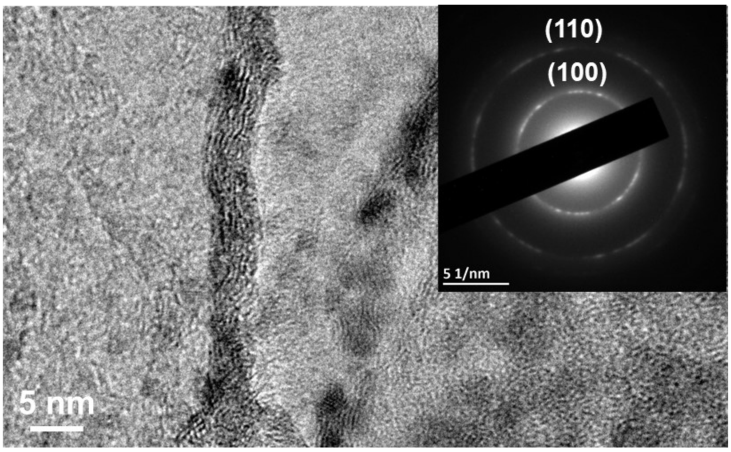

Fig. S9 HRTEM image of the rGO_3 flakes, where the inset shows the typical SAED pattern of the rGO.

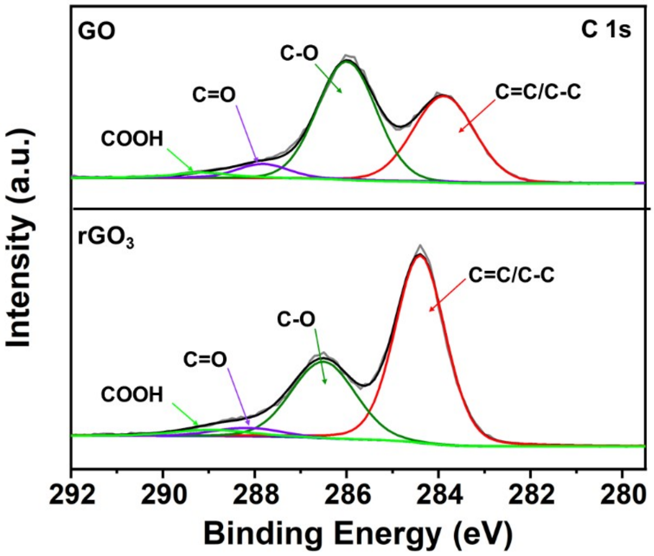

Fig. S10 High-resolution XPS spectra of C 1s of GO and rGO$_3$.

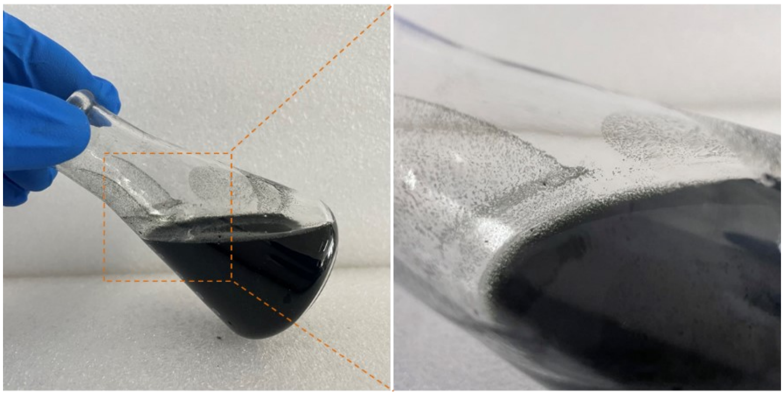

Fig. S11 Optical photographs of the PD-rGOMX dispersion before vacuum filtration.

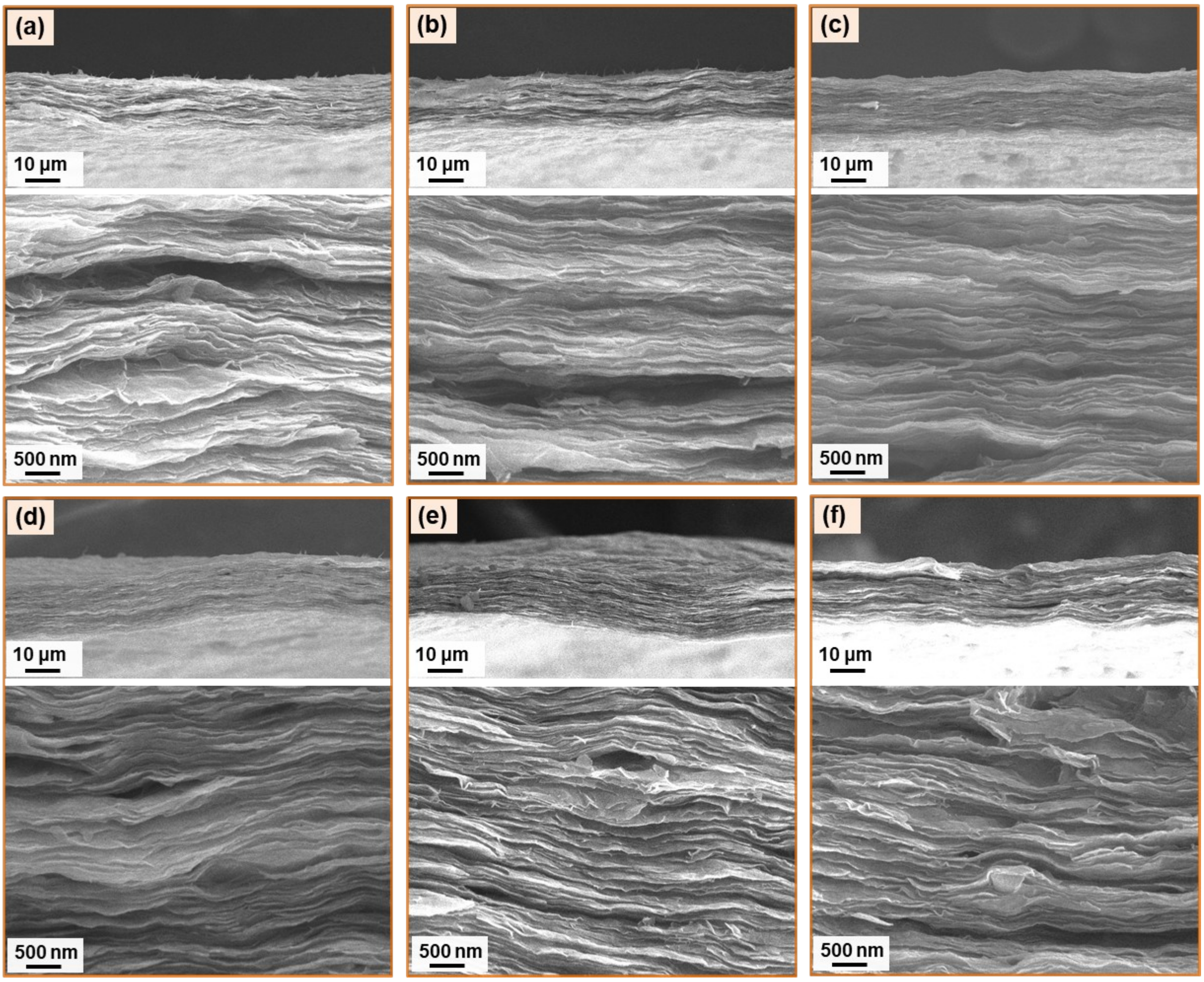

Fig. S12 Fracture surfaces SEM images of PD-rGOMX films with different MXene contents, a) 20 wt%, b) 40 wt%, c) 50 wt%, d) 60 wt%, e) 70 wt%, f) 80 wt%.

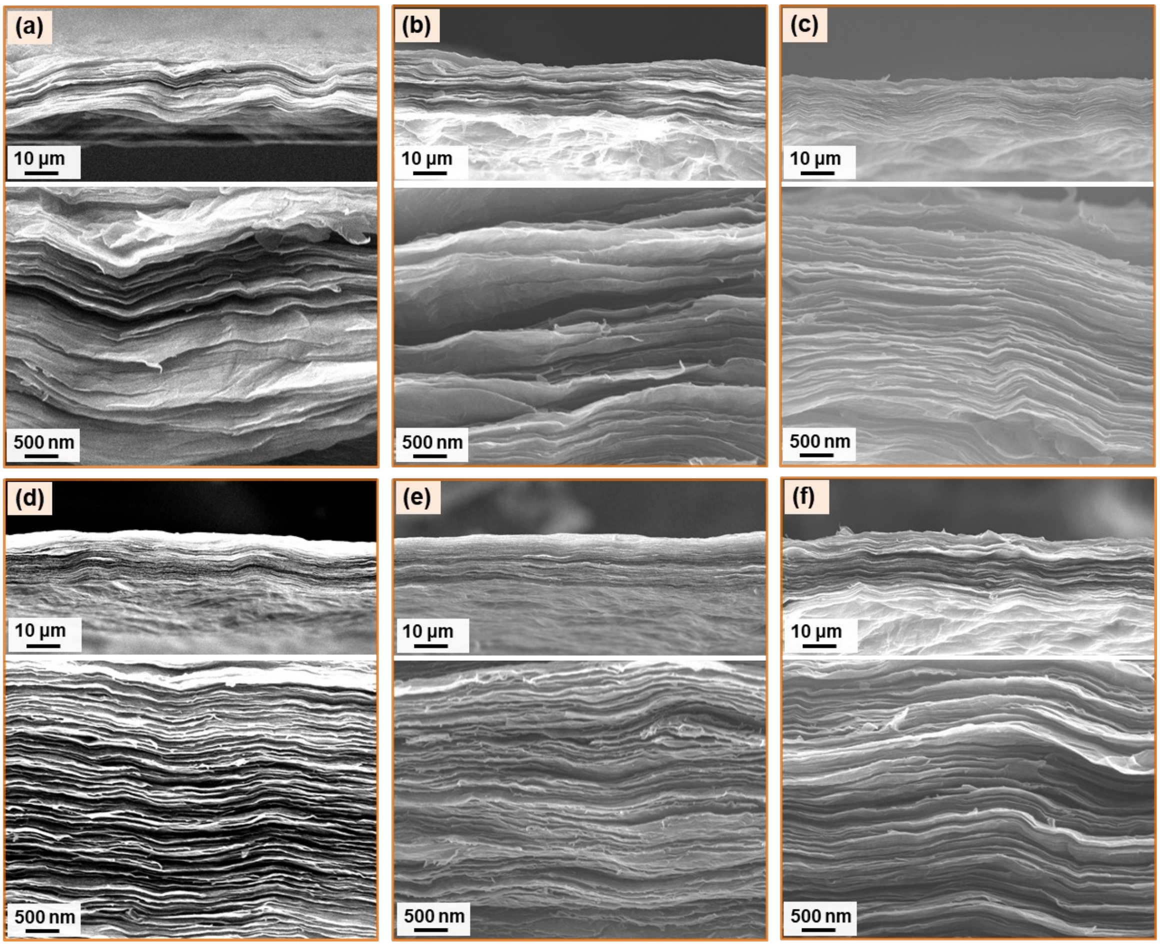

Fig. S13 Fracture surfaces SEM images of a) GO film, b-f) rGO_1-rGO_5 films, respectively.

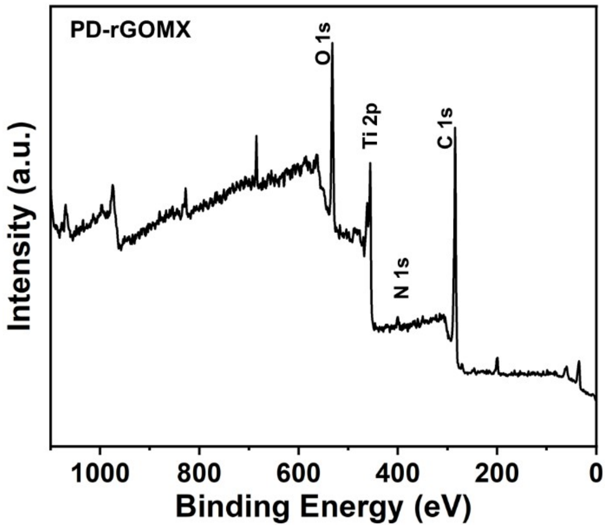

Fig. S14 XPS spectra of the PD-rGOMX.

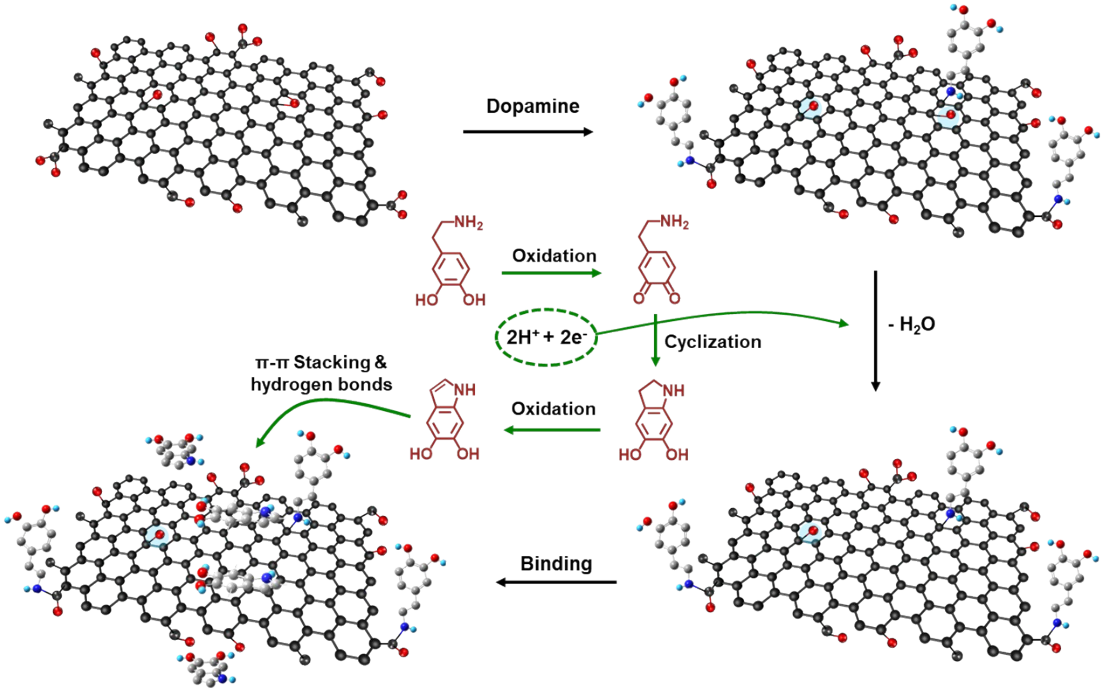

Fig. S15 Schematic illustration of further reduction of rGO by PDA treatment. PDA is bound to rGO through covalent bonds, hydrogen bonds, π-π stacking, etc.

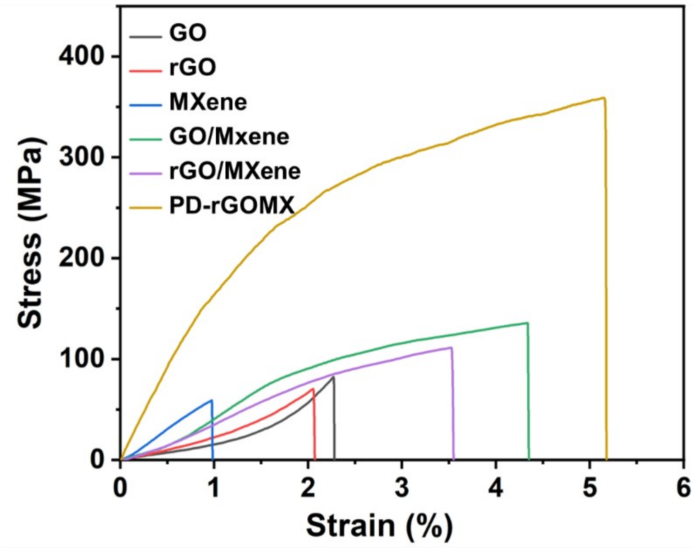

Fig. S16 Stress–strain curves of GO, rGO, MXene, GO/MXene, rGO/MXene and PD-rGOMX films.

Table S3. Comparison of the tensile strength, toughness, and electrical conductivity of PD-rGOMX film in our study with the MXene-based or graphene-based films from others' work.

Number	Samples	Tensile strength (MPa)	Toughness (MJ m^{-3})	Electrical conductivity (S cm^{-1})	Ref.
1	**PD-rGOMX**	**358.7**	**15.2**	**3693**	**This work**
2	MXene/CNF/PDA	237.1	10.9	0	[11]
3	MXene	-	-	3120	[12]
4	CNTs/MXene/Cellulose	97		2506.6	[13]
5	MXene/BCNF	406	15.3	2848	[1]
6	ANF-MXene/AgNW	235.9	-	922	[14]
7	ANF/MXene	232	13.4	879	[15]
8	PEDOT:PSS/MXene	38.6	-	1026.2	[16]

9	PU/MXene	100	3	2897.4	[17]
10	MXene/CNF	112.5	2.7	621	[18]
11	MXene/ANF	300.5	5.3	3661	[19]
12	$Ti_3C_2T_x$/TOCNF	212	5.5	2837	[20]
13	$Ti_3C_2T_x$/CNF	135.4	1.2	739.4	[21]
14	BCs/MXene	532.87	-	509.8	[22]
15	MXene@SnS_2/CNF	78.3	-	786	[23]
16	PVDF/MXene	23	-	214.6	[24]
17	$Ti_3C_2T_x$/PVA	30	-	220	[25]
18	MXene/Cellulos	25.7	-	3573	[26]
19	d-$Ti_3C_2T_x$/ANF	197.4	-	0.295	[27]
20	$Ti_3C_2T_x$/PEDOT:PSS	13.71		340.5	[28]
21	MXene/rGO	-	-	2261	[29]
22	PDA/rGO	178.96	-	0	[30]
23	PVA/rGO	188.9	2.52	52.65	[31]
24	NFC/rGO	315	9.8	163	[32]
25	rGO/PAPB	382	7.5	337	[33]
26	rGO/CNC	419.4	11	152.4	[34]
27	rGO/PAAP	112	1.7	21	[35]
28	rGO/PVA/MMT	356	7.5	136.4	[36]
29	GO/MMT/SPVA	250	-	326	[37]
30	rGO/HPC/Cu	274.3	6.7	127.7	[38]
31	CNa/GO	58	-	$<6\times10^{-4}$	[39]

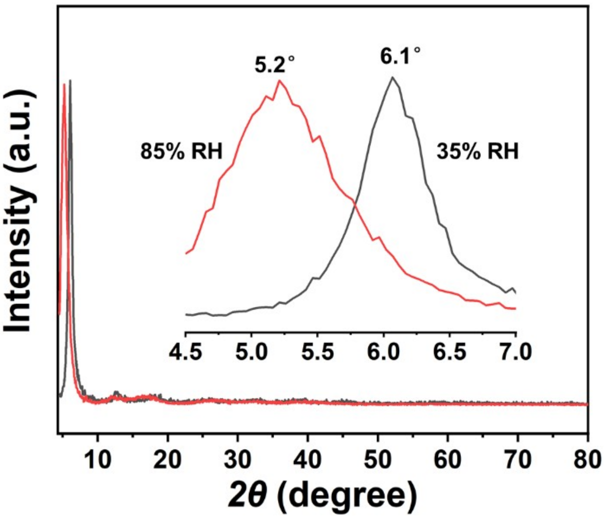

Fig. S17 XRD patterns of the PD-rGOMX at different relative humidities (85% versus 35% RH).

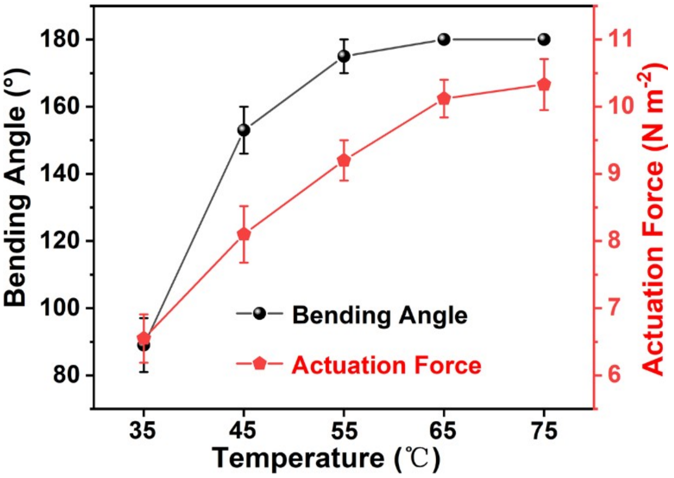

Fig. S18 Bending angles and actuation forces of the PD-rGOMX films (80 wt% MXene) under different water temperatures.

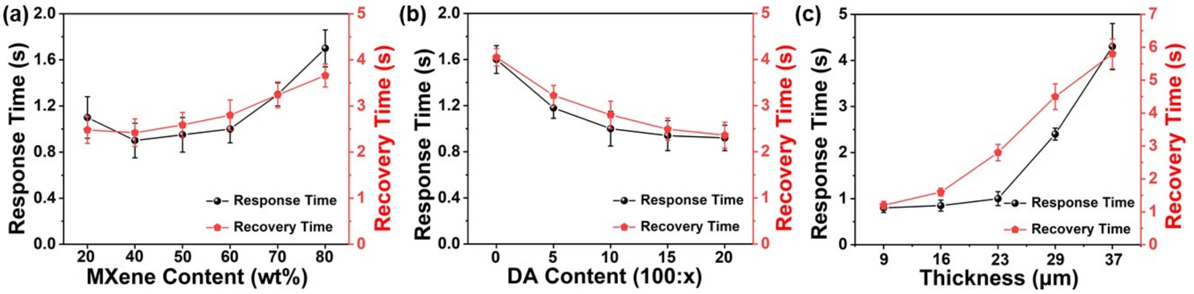

Fig. S19 Response/recovery time of the PD-rGOMX films with a) different MXene content, b) DA content, and c) thickness.

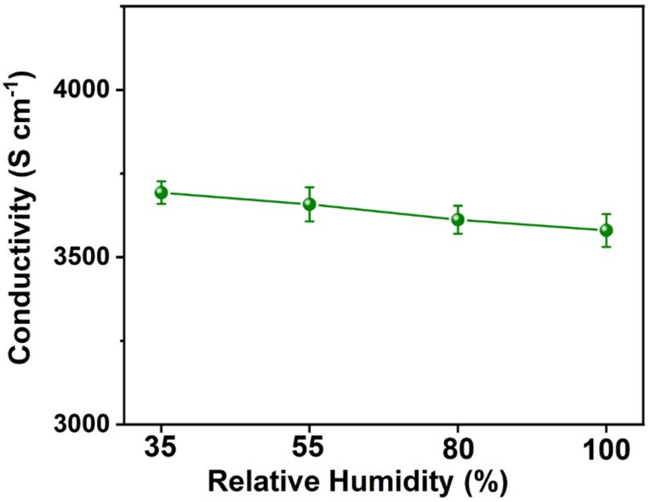

Fig. S20 The effect of relative humidity on the conductivity of the PD-rGOMX film at room temperature. The film has the MXene content of 60 wt%, mass ratio of rGO/MXene:DA as 100:10.

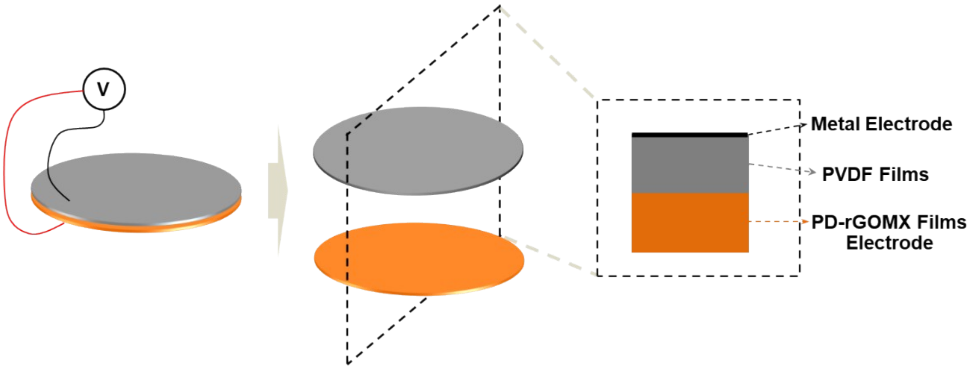

Fig. S21 Schematic diagram showing the structure of our MDG. Specifically, we coupled a piezoelectric polyvinylidene fluoride (PVDF) film (thickness 24 μm) with a PD-rGOMX actuator (thickness 23 μm) to prepare a moisture-driven generator (MDG). It is worth mentioning that we omitted the surface metallization process of the piezoelectric element due to the high conductivity of the PD-rGOMX film, and the PD-rGOMX film acts as an electrode and a driving layer at the same time (only one side of the PVDF film is metalized).

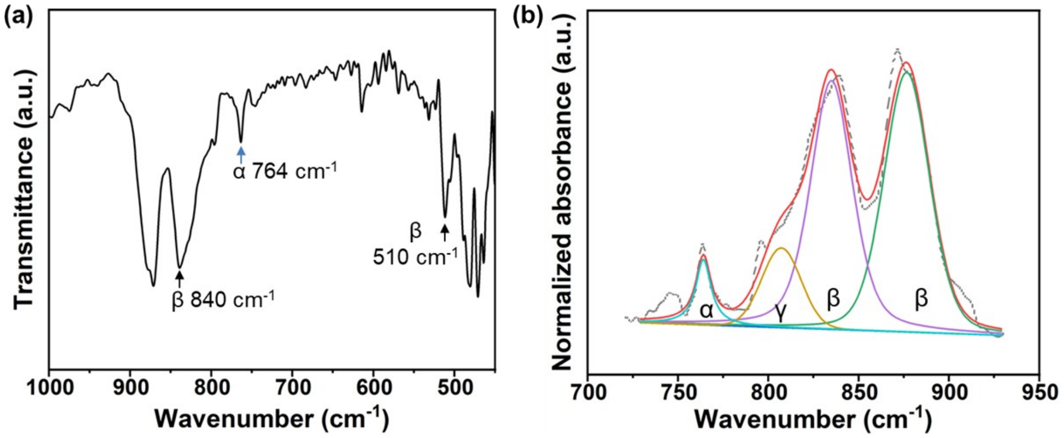

Fig. S22 (a) FTIR spectra of PVDF film. (b) The curve deconvolution of FTIR spectra in 700–950 cm^{-1} range of PVDF film. The absorption of PVDF films at 510 and 840 cm^{-1} is attributed to the β-phase absorption band of the all-trans conformation, and the absorption at 764 cm^{-1} is attributed to the α-phase absorption band of the helical conformation.[40] Deconvolution of the FTIR spectra of PVDF films in the range of 700-950 cm^{-1}, the calculated β-crystallinity is about 82%.

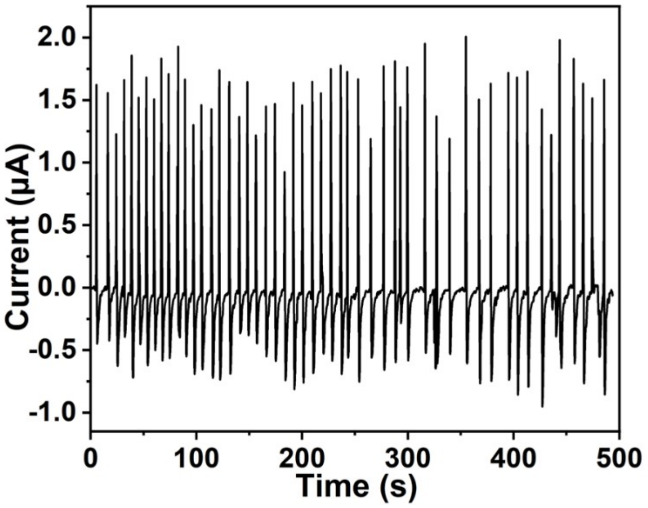

Fig. S23 The real-time current signal produced by the MDG on a 1 MΩ resistor.

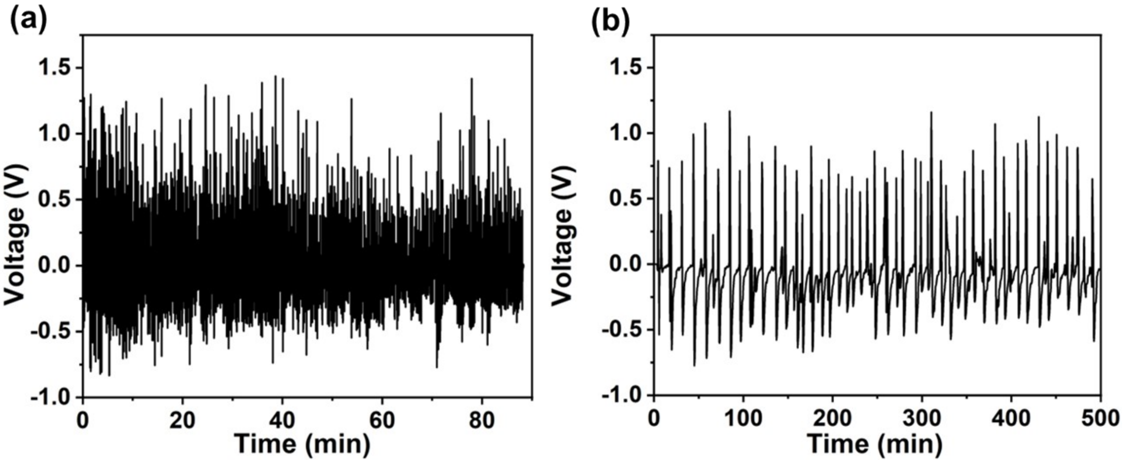

Fig. S24 (a) Real-time voltage output of MEG for about 500 consecutive bending deformations. (b) Continuous voltage output of MEG after 5 months of storage in a laboratory environment. The laboratory temperature is maintained at 15-25°C all year round, and the composite film is stored in a sealed bag and placed at room temperature.

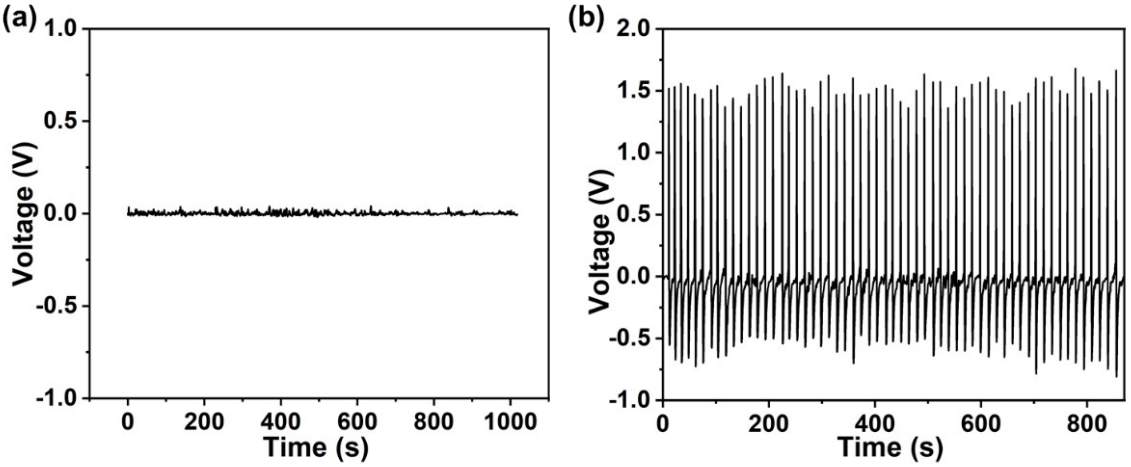

Fig. S25 Output voltage signal by the bare PVDF element without PD-rGOMX actuator. a) Voltage-time signal when PVDF element rests on wet nylon mesh. b) Voltage-time signal at deformation frequency and bending curvature of PVDF similar to MEG.

Reference

1. L. Yang, J. Cui, L. Zhang, X. Xu, X. Chen and D. Sun, *Adv. Funct. Mater.*, 2021, **31**, 2101378.
2. Y. Kang, J. Liu, S. Yin, Y. Jiang, X. Feng, J. Wu, Y. Zhang, A. Chen, Y. Zhang and L. Shao, *ACS Nano*, 2020, **14**, 3059-3074.
3. D. Luo, G. Zhang, J. Liu and X. Sun, *J. Phys. Chem. C*, 2011, **115**, 11327-11335.
4. J. Wu, Y. Wei, H. Ding, Z. Wu, X. Yang, Z. Li, W. Huang, X. Xie, K. Tao and X. Wang, *ACS Appl. Mater. Interfaces*, 2020, **12**, 20623-20632.
5. C. Chen, Y.-C. Chen, Y.-T. Hong, T.-W. Lee and J.-F. Huang, *Chem. Eng. J.*, 2018, **352**, 188-197.
6. K. K. H. De Silva, H. H. Huang, R. K. Joshi and M. Yoshimura, *Carbon*, 2017, **119**, 190-199.
7. S. Park, J. An, I. Jung, R. D. Piner, S. J. An, X. Li, A. Velamakanni and R. S. Ruoff, *Nano Lett.*, 2009, **9**, 1593-1597.
8. Y. Xu, H. Bai, G. Lu, C. Li and G. Shi, *J. Am. Chem. Soc.*, 2008, **130**, 5856-5857.
9. S. Stankovich, D. A. Dikin, R. D. Piner, K. A. Kohlhaas, A. Kleinhammes, Y. Jia, Y. Wu, S. T. Nguyen and R. S. Ruoff, *Carbon*, 2007, **45**, 1558-1565.
10. M. J. Fernández-Merino, L. Guardia, J. I. Paredes, S. Villar-Rodil, P. Solís-Fernández, A. Martínez-Alonso and J. M. D. Tascón, *J. Phys. Chem. C*, 2010, **114**, 6426-6432.
11. J. Cao, Z. Zhou, Q. Song, K. Chen, G. Su, T. Zhou, Z. Zheng, C. Lu and X. Zhang, *ACS Nano*, 2020, **14**, 7055-7065.
12. J. Wang, Y. Liu, Z. Cheng, Z. Xie, L. Yin, W. Wang, Y. Song, H. Zhang, Y. Wang and Z. Fan, *Angew. Chem. Int. Ed.*, 2020, **59**, 14029-14033.
13. W. Cao, C. Ma, S. Tan, M. Ma, P. Wan and F. Chen, *Nano-Micro Letters*, 2019, **11**.
14. Z. Ma, S. Kang, J. Ma, L. Shao, Y. Zhang, C. Liu, A. Wei, X. Xiang, L. Wei and J. Gu, *ACS Nano*, 2020, **14**, 8368-8382.
15. C. Weng, T. Xing, H. Jin, G. Wang, Z. Dai, Y. Pei, L. Liu and Z. Zhang, *Composites Part A: Applied Science and Manufacturing*, 2020, **135**, 105927.
16. Y.-J. Wan, X.-M. Li, P.-L. Zhu, R. Sun, C.-P. Wong and W.-H. Liao, *Compos. Part A Appl. Sci. Manuf.*, 2020, **130**, 105764.
17. Z. Liu, W. Wang, J. Tan, J. Liu, M. Zhu, B. Zhu and Q. Zhang, *J. Mater. Chem. C*, 2020, **8**, 7170-7180.
18. B. Zhou, Z. Zhang, Y. Li, G. Han, Y. Feng, B. Wang, D. Zhang, J. Ma and C. Liu, *ACS Appl. Mater. Interfaces*, 2020, **12**, 4895-4905.
19. C. Lei, Y. Zhang, D. Liu, K. Wu and Q. Fu, *ACS Appl. Mater. Interfaces*, 2020, **12**, 26485-26495.
20. Z. Zhan, Q. Song, Z. Zhou and C. Lu, *J. Mater. Chem. C*, 2019, **7**, 9820-9829.
21. W.-T. Cao, F.-F. Chen, Y.-J. Zhu, Y.-G. Zhang, Y.-Y. Jiang, M.-G. Ma and F. Chen, *ACS Nano*, 2018, **12**, 4583-4593.
22. C. Ma, W.-T. Cao, W. Zhang, M.-G. Ma, W.-M. Sun, J. Zhang and F. Chen, *Chem. Eng. J.*, 2021, **403**, 126438.
23. C. Cai, W. Zhou and Y. Fu, *Chem. Eng. J.*, 2021, **418**, 129275.

24. Y. Li, B. Zhou, Y. Shen, C. He, B. Wang, C. Liu, Y. Feng and C. Shen, *Compos. Part B Eng.*, 2021, **217**, 108902.
25. Z. Ling, C. E. Ren, M.-Q. Zhao, J. Yang, J. M. Giammarco, J. Qiu, M. W. Barsoum and Y. Gogotsi, *Proc. Natl. Acad. Sci. U. S. A*, 2014, **111**, 16676-16681.
26. M. Zhu, X. Yan, H. Xu, Y. Xu and L. Kong, *Ceram. Int.*, 2021, **47**, 17234-17244.
27. F. Xie, F. Jia, L. Zhuo, Z. Lu, L. Si, J. Huang, M. Zhang and Q. Ma, *Nanoscale*, 2019, **11**, 23382-23391.
28. R. Liu, M. Miao, Y. Li, J. Zhang, S. Cao and X. Feng, *ACS Appl. Mater. Interfaces*, 2018, **10**, 44787-44795.
29. J. Yan, C. E. Ren, K. Maleski, C. B. Hatter, B. Anasori, P. Urbankowski, A. Sarycheva and Y. Gogotsi, *Adv. Funct. Mater.*, 2017, **27**.
30. Y. Tian, Y. Cao, Y. Wang, W. Yang and J. Feng, *Adv. Mater.*, 2013, **25**, 2980-2983.
31. Y.-Q. Li, T. Yu, T.-Y. Yang, L.-X. Zheng and K. Liao, *Adv. Mater.*, 2012, **24**, 3426-3431.
32. J. Duan, S. Gong, Y. Gao, X. Xie, L. Jiang and Q. Cheng, *ACS Appl. Mater. Interfaces*, 2016, **8**, 10545-10550.
33. M. Zhang, L. Huang, J. Chen, C. Li and G. Shi, *Adv. Mater.*, 2014, **26**, 7588-7592.
34. Y. Gao, H. Xu and Q. Cheng, *Adv. Mater. Interfaces*, 2018, **5**, 1800145.
35. S. Ye, B. Chen, D. Hu, C. Liu and J. Feng, *Chemnanomat*, 2016, **2**, 816-821.
36. P. Ming, Z. Song, S. Gong, Y. Zhang, J. Duan, Q. Zhang, L. Jiang and Q. Cheng, *J. Mater. Chem. A*, 2015, **3**, 21194-21200.
37. G. He, M. Xu, J. Zhao, S. Jiang, S. Wang, Z. Li, X. He, T. Huang, M. Cao, H. Wu, M. D. Guiver and Z. Jiang, *Adv. Mater.*, 2017, **29**, 1605898.
38. Q. Zhang, S. Wan, L. Jiang and Q. Cheng, *Sci. China Technol. Sci.*, 2017, **60**, 758-764.
39. R. Castaldo, G. C. Lama, P. Aprea, G. Gentile, V. Ambrogi, M. Lavorgna and P. Cerruti, *Adv. Funct. Mater.*, 2019, **29**.
40. T. Li, M. Qu, C. Carlos, L. Gu, F. Jin, T. Yuan, X. Wu, J. Xiao, T. Wang, W. Dong, X. Wang and Z.-Q. Feng, *Adv. Mater.*, 2021, **33**, 2006093.